AGU PUBLICATIONS

JGR

Journal of Geophysical Research: Solid Earth

RESEARCH ARTICLE

10.1002/2014JB011718

Key Points:
- We perform a systematic classification of nonlinear elastic behavior in rocks
- Two physical mechanisms can describe the nonlinear elasticity of these rocks

Correspondence to:
J. Rivière,
riviere_jacques@yahoo.fr

Citation:
Rivière, J., P. Shokouhi, R. A. Guyer, and P. A. Johnson (2015), A set of measures for the systematic classification of the nonlinear elastic behavior of disparate rocks, *J. Geophys. Res. Solid Earth*, *120*, doi:10.1002/2014JB011718.

Received 26 OCT 2014
Accepted 20 FEB 2015
Accepted article online 25 FEB 2015

A set of measures for the systematic classification of the nonlinear elastic behavior of disparate rocks

Jacques Rivière[1], Parisa Shokouhi[2], Robert A. Guyer[1,3], and Paul A. Johnson[1]

[1]Earth and Environmental Sciences, Los Alamos National Laboratory, Los Alamos, New Mexico, USA, [2]Department of Civil and Environmental Engineering, Pennsylvania State University, University Park, Pennsylvania, USA, [3]Department of Physics, University of Nevada, Reno, Reno, Nevada, USA

Abstract Dynamic acoustoelastic testing is performed on a set of six rock samples (four sandstones, one soapstone, and one granite). From these studies at 20 strain levels $10^{-7} < \epsilon < 10^{-5}$, four measures characterizing the nonlinear elastic response of each sample are found. Additionally, each sample is tested with nonlinear resonant ultrasonic spectroscopy and a fifth measure of nonlinear elastic response is found. These five measures of the nonlinear elastic response of the samples (approximately $3 \times 6 \times 20 \times 5$ numbers as each measurement is repeated 3 times) are subjected to careful analysis using model-independent statistical methods, principal component analysis, and fuzzy clustering. This analysis reveals differences among the samples and differences among the nonlinear measures. Four of the nonlinear measures are sensing much the same physical mechanism in the samples. The fifth is seeing something different. This is the case for all samples. Although the same physical mechanisms (two) are operating in all samples, there are distinctive features in the way the physical mechanisms present themselves from sample to sample. This suggests classification of the samples into two groups. The numbers in this study and the classification of the measures/samples constitute an empirical characterization of rock nonlinear elastic properties that can serve as a valuable testing ground for physically based theories that relate rock nonlinear elastic properties to microscopic elastic features.

1. Introduction

Knowledge of the nonlinear elastic properties of a mechanical system makes it possible to assess the behavior of the system as it is stressed [*Guyer and Johnson*, 2009]. Examples, for geophysical and civil engineering applications, include the prediction of wellbore breakout [*Bouchaala et al.*, 2011], monitoring the integrity of formations used to sequester carbon [*Bouchaala et al.*, 2011], assessing the mechanical trajectory of a reservoir, monitoring thermal damage to rock in nuclear waste storage [*Payan et al.*, 2007], and probing concrete integrity [*Van Den Abeele and De Visscher*, 2000; *Van Den Abeele et al.*, 2009]. Dynamic acoustoelastic testing (DAET) allows one to determine the nonlinear elastic properties of a mechanical system with accuracy and relative ease. DAET is a pump-probe scheme in which a high-frequency (HF) elastic wave pulse probes the state of a mechanical system that is set by a low-frequency (LF) elastic wave, the pump. For the pump P we use the fundamental compressional mode of a rod-shaped sample driven to strain amplitudes $10^{-7} \leq \epsilon_P < 10^{-5}$. The probe ($p$) is a HF pulse (of low strain amplitude, $\epsilon_p \simeq 10^{-7}$) that tests the state of the sample at all phases of the pump strain field, i.e., in both compression and tension. From the behavior of the probe a complete description of the nonlinear elastic properties of the sample is obtained, e.g., hysteresis, tension/compression asymmetry, and nonlinear elastic constants.

DAET offers advantages over several existing methods. In contrast to static acoustoelastic testing, in which the "pump" (a mechanical compression or tension press) sets an $\omega \to 0$ strain field in the sample [*Winkler and McGowan*, 2004], DAET determines the response of the sample to both tension and compression [*Renaud et al.*, 2009, 2010, 2011, 2013a, 2013b, 2014]. Furthermore, dynamic acoustoelasticity is of the sample at a finite pump frequency, $\omega > 0$, where the important "conditioning" and "slow dynamics" effects are present in the state which the pump sets [*TenCate and Shankland*, 1996; *TenCate*, 2011; *Renaud et al.*, 2013a]. In contrast to nonlinear resonant ultrasonic spectroscopy (NRUS) [*Pasqualini et al.*, 2007; *Van Den Abeele et al.*, 2000a] and harmonic-based techniques [*Van Den Abeele et al.*, 2000b], which measure average responses over all phases, by testing the state of the sample at all phases, DAET allows us to obtain a more complete picture of the nonlinear elastic behavior of the sample.

Table 1. Sample Description[a]

Name	Composition	Density (g/cm^3)	Length, L (cm)	Longitudinal Velocity, c (km/s)	Resonance Frequency (kHz)
Berea sandstone (USA)	Fine-grained argillaceous micaceous sandstone	2.2	15	2.8	4.6
Red Meule sandstone (France)	Fine-grained argillaceous micaceous sandstone	2.2	12	3.1	5.4
Sander sandstone (Germany)	Subarkose sandstone	2.2	17	2.7	4.4
Pietra Serena sandstone (Italy) (Italy)	Graywacke sandstone	2.6	17	3.3	5.2
Grunnes Nidaros soapstone (Norway) (Norway)	Talc schist	2.9	17	4.8	6.3
Berkeley Blue Granite (USA)	Medium-grained anorthosite	2.7	15.6	3.4	4.2

[a]All samples are rod shaped with a diameter of 2.54 cm and length ranging from $L = 12$ to 17 cm.

This paper is the third in a series that develops DAET for geophysical applications. In the first paper of the series the efficacy of the DAET procedure for a large set of geophysical samples was established [*Renaud et al.*, 2012]. In the second paper, a data analysis scheme was introduced that allows one to extract great detail about the nonlinear behavior of a sample from DAET [*Rivière et al.*, 2013]. (This data analysis scheme has applications well beyond the geophysical example used to illustrate its workings.) Here we bring this analysis scheme to data on a set of samples (six rock types) that are subject to 20 pump strain values. To these data we add the results of NRUS testing. We look in detail at the nonlinear measures of the behavior of each sample. Then to develop a description across samples we characterize the behavior of each sample with five nonlinear measures, four describing aspects of the nonlinear elastic behavior gleaned from DAET and the fifth describing the NRUS results. We subject this set of nonlinear measures to statistical analysis using two tools, principal component analysis (PCA) and "fuzzy" clustering (FC). Upon using these tools we can (a) establish the connection of the nonlinear measures to one another, (b) extract two primary nonlinear measures to characterize all of the data, and (c) use these primary nonlinear measures to sort the samples into clusters based on their nonlinear properties. The data analysis to this point has gone forward without the need for a microscopic model of the elastic features responsible for what is observed. We complete the analysis of the data with description of possible microscopic models for our observations.

In section 2, we describe the set of samples, the experimental system, the experimental protocol, and application of the data analysis scheme. In section 3, we present DAET and NRUS results and the organization of the data provided by a statistical analysis using PCA and FC. We discuss the results with an eye toward physical insights in section 4.

2. Materials and Methods

2.1. Samples

The samples used in this study, part of the sample set used in [*Renaud et al.*, 2012], consist of four sandstones (Berea, Red Meule, Sander, and Pietra Serena), one soapstone (Grunnes Nidaros), and one granite (Berkeley Blue). These samples, which include a crystalline rock (granite), a metamorphic rock (soapstone), and four sedimentary rocks (sandstones), offer the opportunity to compare nonlinear behavior across a spectrum of rock types. All samples are rod shaped with a diameter $d = 2.54$ cm. Their length, density, longitudinal velocities as well as resonance frequencies of the first compressional mode are listed in Table 1.

2.2. Experimental Details

2.2.1. DAET Setup

Each sample, cylindrical in shape and in room-dry conditions, is placed upright vertically on the pump, a low-frequency (LF) compressional source, a piezoceramic disk (Figure 1). The probe source, a high-frequency (HF) compressional source, and receiver straddle the sample at height $h = 2$ cm above the piezoceramic disk. A light weight accelerometer, placed on the free surface at the top of the sample, is used to monitor the

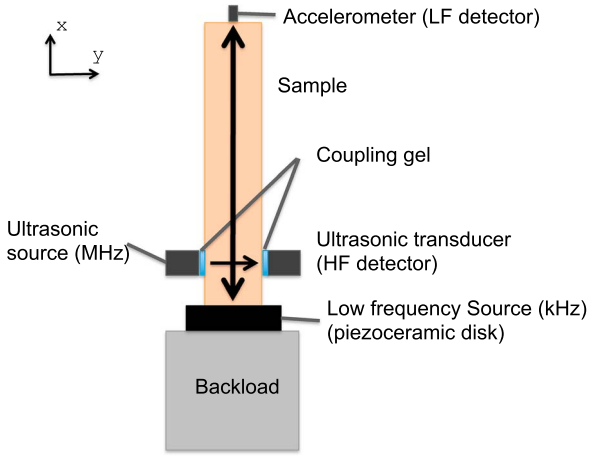

Figure 1. DAET setup. The low-frequency source resonates the sample in its first compressional mode (kHz), fixed free boundary conditions, at various strain amplitudes from 10^{-7} to 10^{-5}. High-frequency pulses at 1 MHz are launched into the sample to probe the sample at a given strain level established by the low-frequency source. An accelerometer placed on the top of the sample allows us to measure the low-frequency strain field. An ultrasonic transducer detects the HF pulses. The NRUS setup is equivalent to the DAET setup, except that only the LF part is kept to resonate the sample in its first compressional mode.

pump displacement/strain field. The essential idea is to have a HF broadcast, from source to receiver, probe the elastic state that is set in the sample by the LF source.

The LF source has a diameter greater than d and creates a strain field $\epsilon_x(x,t)$ in the sample that is primarily a function of x; x is measured upward from the piezoceramic disk. The frequency f_{LF} is the frequency of the lowest compressional resonant mode of the cylinder for fixed free boundary conditions, $f_{LF}=c/(4L)$, i.e., wavelength $\lambda_{LF}=4L$. Here c is the nominal compressional sound speed in the sample, e.g., in Berea sandstone roughly 2800 m/s (Table 1). Thus, for Berea sandstone $f_{LF}\simeq 4.6$ kHz and $\lambda_{LF}=60$ cm. The strain field is sampled at $x=h$ by the HF broadcast that crosses the sample in time, t_{HF}, of order $d/c\simeq 10\mu$s. During the HF wave travel time the LF strain field changes very little, $t_{HF}/T_{LF}=d/(4L)=2.54/60\simeq 0.04$, $T_{LF}=1/f_{LF}$ (taking, for example, the Berea sandstone, L = 15 cm, Table 1). In addition, the width of the HF beam is approximately the diameter of the HF transducer ($d_{HF}=6$ mm). Thus, we can assume that the strain established in the sample by the LF source is spatially constant over the HF beam width ($d_{HF}/\lambda=0.6/60=0.01$). This condition and the condition $t_{HF}<<T_{LF}$ are required in order that the probe shall have a simple experience of the pump as it crosses the sample.

For the case of fixed free boundary conditions, the strain is maximum at $x=0$ and can be estimated from the acceleration measured at the top of the sample using the displacement/strain relation for the lowest compressional mode

$$\epsilon_x(0,t) = -\ddot{u}_x(L,t)/(8\pi L f_{LF}^2). \quad (1)$$

We take the strain at $x = h$ to be the strain at the base, according to results found in *Rivière et al.* [2013].

The HF source is one period of a 1 MHz broadcast. The LF broadcast/detection and the HF broadcast/detection, both sampled at 50 MHz, are controlled by a central clock.

2.2.2. NRUS Setup

A series of nonlinear resonant ultrasound spectroscopy [*Van Den Abeele et al.*, 2000a; *Haupert et al.*, 2011] measurements is conducted on each sample. The apparatus for these measurements is the same as that for the DAET measurements (Figure 1), using only the LF part of the setup. Similar to the DAET measurements, the first compressional mode is used. The drive frequency is swept upward and downward to monitor potential conditioning effects. Upward/downward frequency sweeps are repeated three times, giving a total of six resonance frequency values for each level of LF source amplitude.

2.3. Measurement Protocol

The DAET measurement protocol involves the following steps. At time $t=t_0=0$, the HF source is turned on, sending 1 MHz pulses at a sequence of times $t_j, j=1,\ldots,$. The time between successive pulses, ΔT, is chosen such that the coda signal received in response to the j^{th} pulse decays to zero before sending the $(j+1)^{th}$ pulse. We use $\Delta T\simeq 1$ ms. From the complete signal recorded at the HF receiver we extract the direct wave, i.e., the first period of each received pulse $s(t-t_j)$.

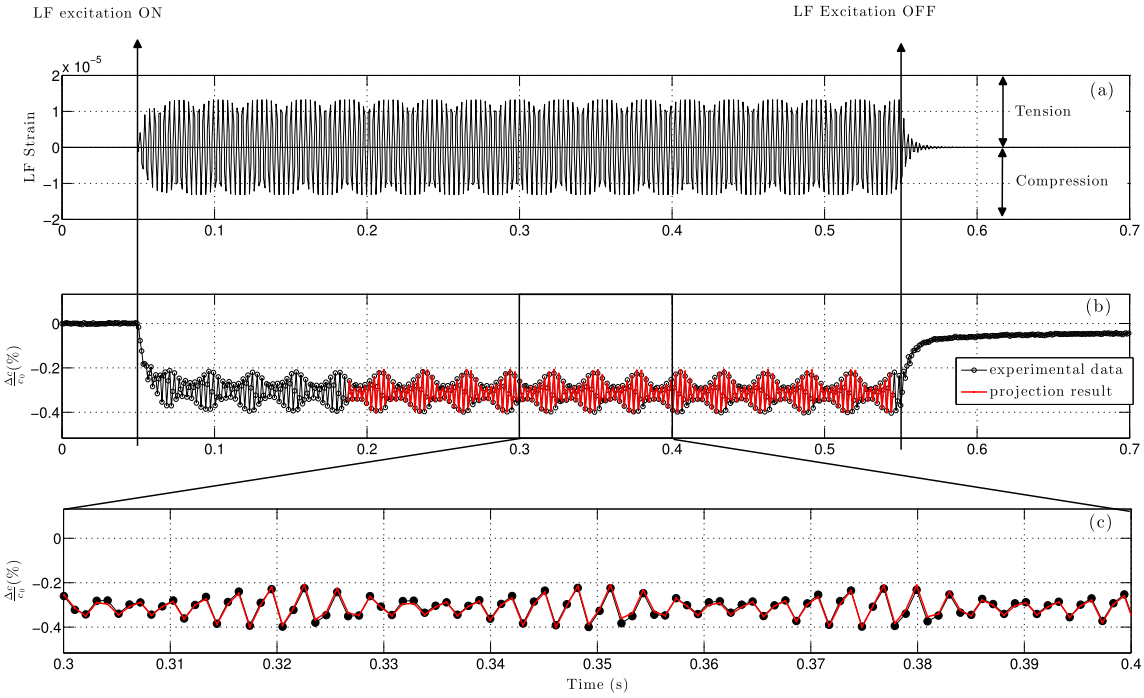

Figure 2. Example of projection procedure. (a) LF strain as a function of time obtained from equation (1). Positive (negative) strain corresponds to the tension (compression) phase. (b) HF velocity change as a function of time extracted using equation (3). Projection result is in red. (c) Zoom of Figure 2b on a shorter time window to observe the good agreement between experimental data and projection result.

The LF source, at frequency ω and amplitude A, is turned on at t_0+ 5 ms, allowing several ultrasonic pulses to propagate across the sample in the absence of LF strain field. The signal at the top of the sample is recorded at times t_i spaced by 0.02 μs (corresponding to the 50 MHz sampling rate). The signal measured at t_i, an acceleration, is related to the displacement field at the top of the sample and to the nominal strain field $\epsilon_x(h, t_i)$ in the sample as described above.

For Berea sandstone, the steady state is reached after roughly 100 ms of LF vibration (Figure 2a). Each pulse $s(t-t_j)$ propagating during the steady state time domain is to be compared to a reference pulse that crosses the sample before the LF source is turned on, e.g., $s(t-t_0)$. The time between successive pulses, ΔT, is chosen to be incommensurate with T_{LF} so that over time the HF broadcasts at the times $\{t_j\}$ sample all phases of the pump strain field.

The first step in the analysis of $s(t - t_j)$ from the steady state time domain is to compare it to the reference pulse $s(t - t_0)$ by using the cross correlation:

$$C(\tau, t_j) = \int_0^\infty s(t - t_0)s(t + \tau - t_j)\mathrm{d}t \tag{2}$$

to determine $\tau_{\max}(t_j)$, the shift in the time of flight of the HF pulse as it crosses the sample at time t_j [*Renaud et al.*, 2009, 2010]. (The shift $\tau_{\max}(t_j)$ is refined by interpolating the peak of the cross-correlation function with a second-order polynomial function to obtain subsample time resolution [*Cespedes et al.*, 1995]. Three points are considered for this interpolation: the maximum of the cross-correlation function and the two adjacent points.) Assuming that dynamic variations in the sample diameter (i.e., the probe path) due to Poisson effect are negligible [*Renaud et al.*, 2011], time of flight shift can be converted into a relative velocity change using the following:

$$\frac{\Delta c}{c}(t_j) = -\frac{\tau_{\max}(t_j)}{t^0_{HF}}, \tag{3}$$

where t^0_{HF} is the time of flight of the reference pulse. Finally, the change in the relative sound speed is associated with the strain field at $x = h$ at the moment of the HF broadcast, i.e., $\frac{\Delta c}{c}(t_j) \Leftrightarrow \epsilon_x(h, t_j)$ where $\epsilon_x(h, t_j)$ is the average of LF strain field at h over $t_j \le t \le t_j + d/c$.

We start the protocol with a pump excitation at amplitude A. We launch this excitation (and the concomittant series of ultrasonic pulses) 10 times with a waiting time of 30 s between launches. This waiting time is chosen long enough to ensure that most of the relaxation has taken place (slow dynamics [*TenCate*, 2011]) but short enough to perform measurements in stable environmental conditions (the slow dynamics may continue for minutes or hours after the sample is perturbed; however, most of the relaxation takes place very rapidly, within the first 10–20 s). The data recorded during the 10 launches is averaged and the averaged data (both pump and probe) are the data we analyze. This protocol, at amplitude A, is repeated 3 times by replacing the HF transducer pair and the coupling gel in order to ensure reproducibility. These three runs (each of 10 launches) are averaged and the error bars presented in section 3 represent 1 standard deviation over the three runs. After completing this measurement protocol at amplitude A, we repeat it for the next pump amplitude. For both the DAET measurements and the NRUS measurements (section 2.2.2), strain space, $10^{-7} < \epsilon < 10^{-5}$, was scanned logarithmically giving equal weight to all strain values. Finally, we note that part of the data related to the Berea sandstone was presented previously [*Rivière et al.*, 2013]. For Berea the sequence of 10 launches was repeated 2 times only and the time between two successive HF pulses was 10 times shorter, $\Delta T \simeq 0.1$ ms instead of 1 ms.

2.4. Signal Analysis: Projection Procedure

The dynamic acoustoelastic experiment allows one to obtain the relative change in the speed of sound $\frac{\Delta c}{c}(t_j)$ as a function of time (Figure 2b) or LF strain (Figure 3). This signal is a down-sampled signal (at the frequency of the HF pulse repetition rate, cf. Figure 2c) that is analyzed with a projection procedure [*Rivière et al.*, 2013]. The method is a dedicated Fourier analysis which consists in projecting the signals onto a series of sine and cosine functions, at frequencies related to the LF drive frequency ω, which have support at the time points t_j, $1 \leq j \leq M$, M is the total number of time points in the steady state time domain at which $\Delta c/c$ is calculated (Figure 2b):

$$\begin{aligned} S_n\left(t_j\right) &= q_n \sin\left(n\omega t_j\right) \\ C_n\left(t_j\right) &= r_n \cos\left(n\omega t_j\right) \end{aligned} \tag{4}$$

where $n = 1, 2, \ldots, N$ and N is chosen according to the harmonic content of the signal, e.g., $N = 11$ for the Berea sample. The amplitudes q_n and r_n are such that these functions are orthonormal:

$$\begin{aligned} \langle S_m | S_p \rangle &= \delta_{m,p} \\ \langle C_m | C_p \rangle &= \delta_{m,p} \\ \langle S_m | C_p \rangle &= 0\ , \end{aligned} \tag{5}$$

where $\delta_{m,p}$ is the Kronecker δ function ($\delta_{m,p} = 1$ if $m = p$, 0 otherwise), $\langle . | . \rangle$ stands for the scalar product, $\langle S_m | S_p \rangle \equiv \sum_{j=1}^{M} S_m\left(t_j\right) S_p\left(t_j\right)$, and q_n and r_n are found using a numerical Gram-Schmidt process [*Rivière et al.*, 2013]. This orthonormalization step is necessary because the initial base of sines and cosines (if one chooses q_n and $r_n = 1$) is not fully orthonormal, due to the small number of time points M ($\simeq 350$).

The analysis yields the representation of $\Delta c/c$ at t_j, denoted $\frac{\Delta c}{c}|_p(t_j)$, given by

$$\left.\frac{\Delta c}{c}\right|_p (t_j) = \sum_{n=1}^{N} a_n S_n\left(t_j\right) + \sum_{n=1}^{N} b_n C_n\left(t_j\right), \tag{6}$$

where coefficients a_n and b_n are

$$\begin{aligned} a_n &= \langle S_n | \frac{\Delta c}{c} \rangle \\ b_n &= \langle C_n | \frac{\Delta c}{c} \rangle. \end{aligned} \tag{7}$$

The coefficients $A_n = a_n q_n$ and $B_n = b_n r_n$ determine how much of the nth harmonic, $\omega_n = n\omega$, is present in the signal. Assuming that the response at the fundamental frequency is a sine function, the amplitude A_1 determines how much of the signal remains in phase with the fundamental. Then, the amplitude B_1 determines how much of the signal is in quadrature. The magnitude $\frac{\Delta c}{c}|_{n\omega} = \sqrt{A_n^2 + B_n^2}$ is used as a measure of harmonic content.

Note that magnitudes $\frac{\Delta c}{c}|_{n\omega}$ average hysteretic behaviors, by summing up the in-phase component and the component that is in quadrature. Performing the separation of both components (as shown for Berea

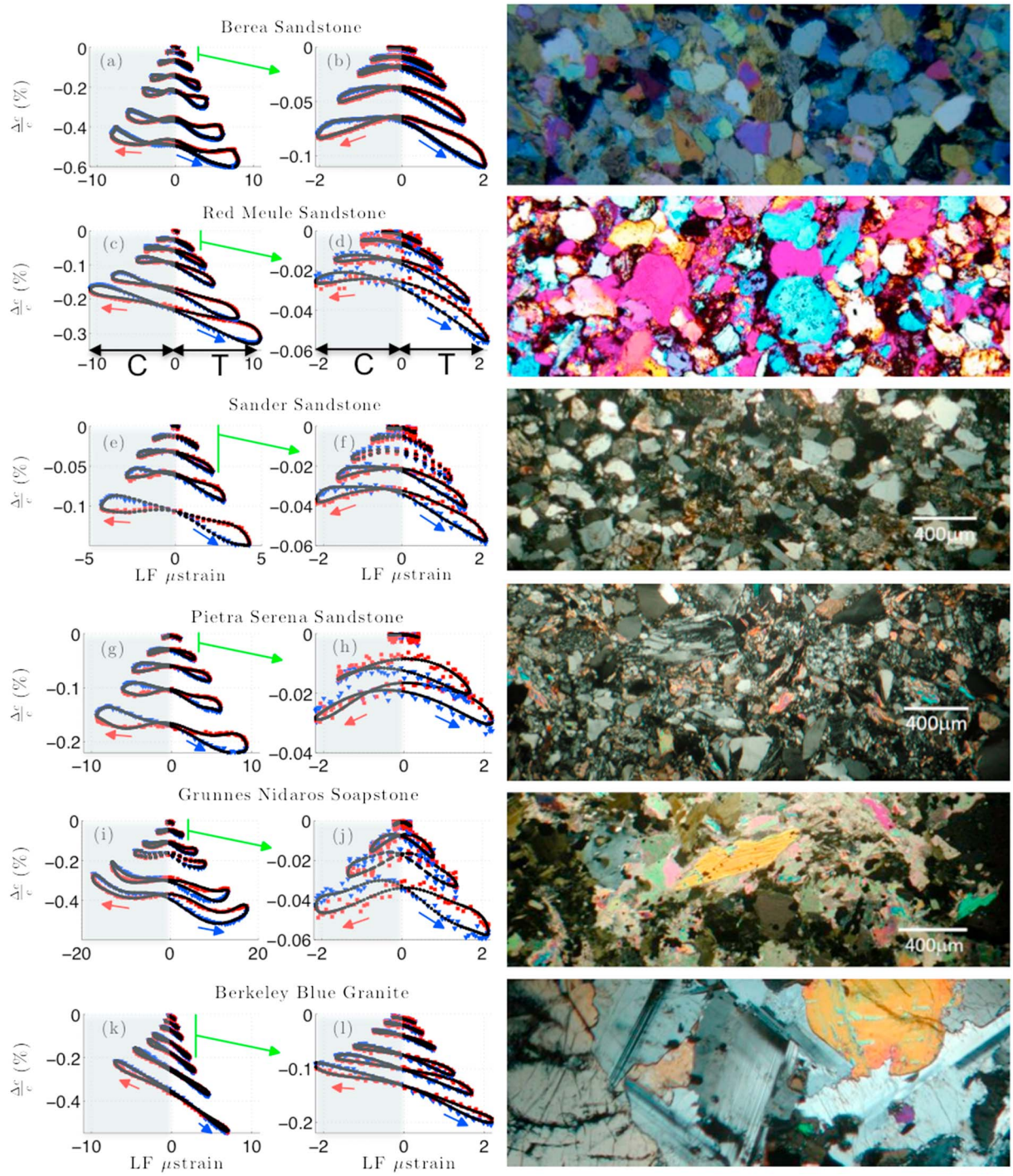

Figure 3. Relative velocity change $\frac{\Delta c}{c}$ as a function of strain $\epsilon_{1\omega}$ for 20 increasing LF strain excitations ranging from 10^{-7} to 10^{-5}. Some amplitudes are removed at several strain levels for clarity. (a and b) Berea sandstone. (c and d) Red Meule sandstone. (e and f) Sander sandstone. (g and h) Pietra Serena sandstone. (i and j) Grunnes Nidaros sandstone. (k and l) Berkeley Blue granite. Zooms are made for strain amplitudes $\leq 2.10^{-6}$ (Figures 3b, 3d, 3f, 3h, 3j, and 3l). Blue triangles (red squares) correspond to increasing (decreasing) strains. Negative strains correspond to the compression phase (C), whereas positive strains correspond to the tension phase (T). The black line shows the result of the Fourier analysis. On the right side, photomicrographs under plane polarized light. Width of the photo is 2.35 mm for Berea sandstone, 3.85 mm for Berkeley blue granite, and 3.1 mm for other samples.

in Figure 5 of *Rivière et al.* [2013]) at all strain amplitudes and for all samples in an automatic manner is not straightforward because of the slight change in f_{LF} (and related phase) at each larger excitation amplitude due to nonlinearity. This could be addressed in future work.

The projection procedure also yields a representation of the pump source strain field at t_j from equation (1):

$$\epsilon_{1\omega}(t_j) = e_S S_1(t_j) + e_C C_1(t_j),\ e_S =< S_1|\epsilon_x(0,t_j) >,\ e_C =< C_1|\epsilon_x(0,t_j) > . \tag{8}$$

The amplitude of the pump source strain field is

$$\epsilon_{1\omega} = \sqrt{(q_1 e_S)^2 + (r_1 e_C)^2}. \tag{9}$$

In section 3, $\frac{\Delta c}{c}|_{n\omega}$ is plotted as a function of $\epsilon_{1\omega}$. In addition to $\frac{\Delta c}{c}|_{n\omega}$, with $n \geq 1$, the $n = 0$ component, $\frac{\Delta c}{c}|_{0\omega}$ (called the *offset*), is found as the average of $\Delta c/c$ in the steady state time domain (see Figure 2b). Because the offset is negative the value $-\frac{\Delta c}{c}|_{0\omega}$ is used in log-log plots.

3. Experimental Results

3.1. Nonlinear Signatures Obtained From DAET

In Figure 2 we show the basic features in the data/analysis. In Figure 2a the pump strain field found from equation (1) is plotted as function of time, positive (negative) strain values correspond to the tension (compression). In Figure 2b the velocity change, $\Delta c/c$ found from equation (3), is shown as a function of time. We observe a reduction in c over about 0.03 s as the sample comes to steady state with the pump drive on and a slow recovery of c from steady state after the pump drive is turned off (the phenomenon known as "slow dynamics" [*TenCate*, 2011]). Representation of the $\Delta c/c$ data using the projection procedure is shown in red in Figures 2b and 2c. In this paper we are concerned only with the behavior of the samples in the steady state time domain. Each sample was brought to steady state at 20 values of the LF strain in the interval 10^{-7} to 10^{-5} and $\Delta c/c$ measured. We show a sampling of all of the $\Delta c/c$ data in the form $\Delta c/c$ versus $\epsilon_{1\omega}$ in Figures 3a–3l. Also shown in the figure, for each $\Delta c/c$ curve, is the representation of $\Delta c/c$ using the projection procedure (black curves). The curves $\Delta c/c$ versus $\epsilon_{1\omega}$ are called the *nonlinear signatures*.

For all of the sandstones and the soapstone at intermediate strain amplitudes (10^{-6}), we observe softening maxima for strain extrema, i.e., the velocity is minimal when the sample reaches its maximal compression and tension, while it is maximum when the strain is zero. On increasing the amplitude from 10^{-6} to 10^{-5}, the nonlinear signatures progressively evolve such that the velocity is maximum during the compression phase and minimum during the tension phase (the curvature observed at intermediate amplitude disappears at larger amplitudes). As opposed to soapstone and sandstones, the velocity for granite is always a maximum during the compression phase and minimal during the tension phase, regardless of the strain amplitude. Hysteresis also seems to be smaller for granite than for other samples.

3.2. Decomposing the Nonlinear Signatures

The projection representation of $\Delta c/c$ allows us to decompose the nonlinear signatures into components having frequencies related to the pump frequency ω. We show the amplitudes $\frac{\Delta c}{c}|_{n\omega} = \sqrt{A_n^2 + B_n^2}$ as a function of $\epsilon_{1\omega}$ in Figure 4. We note that for all samples, the $n = 0$ component (the offset $\frac{\Delta c}{c}|_{0\omega}$) is largest. There are several qualitative properties of note. (1) The $\frac{\Delta c}{c}|_{2\omega}$ components (red curves) are larger than $\frac{\Delta c}{c}|_{1\omega}$ components (blue curves) for several samples (Berea sandstone, Pietra Serena sandstone, and Grunnes Nidaros Soapstone) at intermediate strain amplitudes ($\simeq 10^{-6}$). This observation is equivalent to having a third harmonic larger than a second harmonic in wave mixing [*Meegan et al.*, 1993]. (2) Higher harmonic content ($n \geq 3$) emerges from the noise for strains above about 10^{-6}. For these harmonics we have $\frac{\Delta c}{c}|_{4\omega} > \frac{\Delta c}{c}|_{3\omega}$ and $\frac{\Delta c}{c}|_{6\omega} > \frac{\Delta c}{c}|_{5\omega}$, i.e., preferential generation of odd harmonics ($A_{5w} > A_{4w}$, $A_{7w} > A_{6w}$) [*Meegan et al.*, 1993; *Van Den Abeele et al.*, 1997, 2000a; *McCall and Guyer*, 1994]. (3) Berkeley blue Granite can be adequately described with just three components, $N = 2$ only, i.e., the fit of the experimental results using the projection representation is found to be best with $N = 2$ [*Rivière et al.*, 2013].

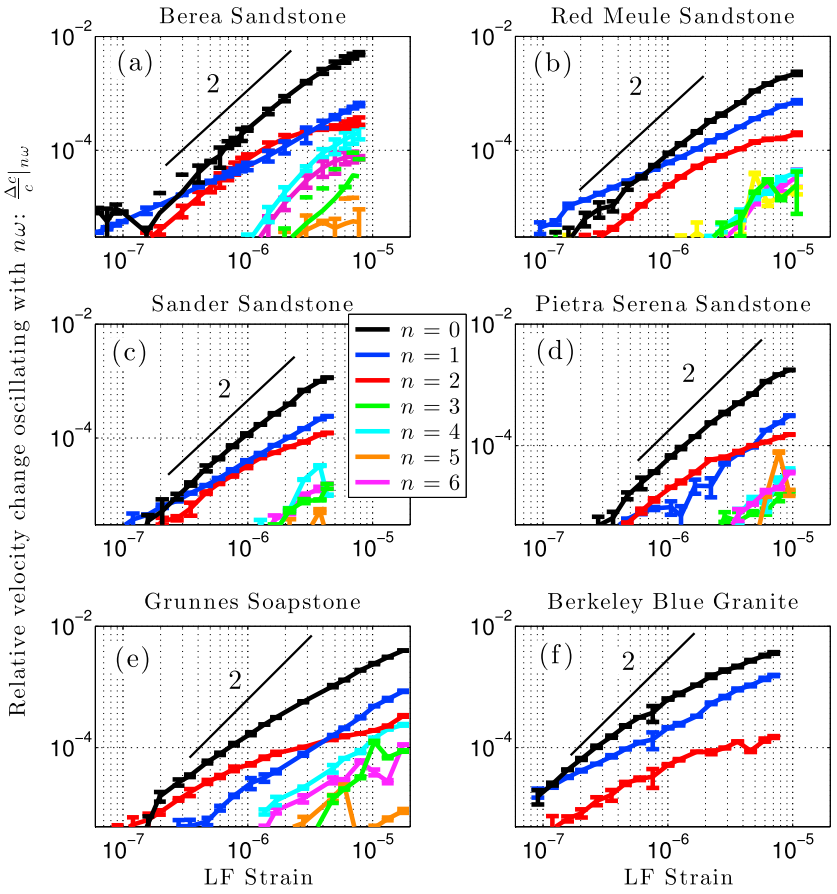

Figure 4. Amplitude dependence extracted from the projection procedure. Note that $\frac{\Delta c}{c}|_{0\omega}$ corresponds to the offset, i.e., the average change in velocity during the LF steady state excitation. Because the offset is negative, $-\frac{\Delta c}{c}|_{0\omega}$ is actually represented in the log-plot. (a) Berea sandstone. (b) Red Meule sandstone. (c) Sander sandstone. (d) Pietra Serena sandstone. (e) Grunnes Nidaros sandstone. (f) Berkeley Blue granite.

It is of interest to see how the results from the projection procedure vary across materials. To this end, in Figures 5a–5c, we show the data that is in Figure 4 sorted by harmonic number for $n = 0, 1, 2$. In addition to the harmonic content we show the hysteresis area in Figure 5d (see Appendix A). The four measures of the probe response to the pump shown in Figures 5a–5d, $\frac{\Delta c}{c}$ versus $\epsilon_{1\omega}$, will be used extensively in the discussion below. To facilitate this discussion we adopt the following language: $\frac{\Delta c}{c}|_{0\omega}$ is the offset, $\frac{\Delta c}{c}|_{1\omega}$ is the *slope*, $\frac{\Delta c}{c}|_{2\omega}$ is the *curvature*, and $\frac{\Delta c}{c}|_{H}$ is the *area*. In Figures 5a–5d, we can observe (1) the amplitude of these measures and (2) how these measures evolve with strain. Take the offset as an example. On using the fitting function $\log(-(\Delta c/c)_{0\omega}) = \nu \log(\epsilon_{1\omega}) + \log(a)$ we find a, the amplitude of the offset and ν which tells us how on average the offset scales with strain. As pointed out in previous studies [*Xu et al.*, 1998; *Van Den Abeele et al.*, 2000b; *Scalerandi et al.*, 2014], analyzing ν values among samples can help classify different nonlinear mechanisms, while a values tell us how much of a mechanism is present in each sample. For instance, it has been reported that the exponent ν increases from 1 up to 3 with mechanical or thermal loadings in concrete, as the damage properties evolve from intrinsic damage (closed cracks, grain-grain contacts, dislocations,...) to macrodamage (open cracks) *Scalerandi et al.* [2014].

In Figure 5a ($n = 0$), Berkeley blue granite and Berea sandstone exhibit the largest offset (large a values). In Figure 5b ($n = 1$) the whole set of samples exhibit roughly a linear dependence of $\frac{\Delta c}{c}|_{1\omega}$ on strain ($\nu \simeq 1$). The measure $\frac{\Delta c}{c}|_{1\omega}$ for Berkeley blue granite is almost 1 order of magnitude larger than for the other samples (large a value). In Figure 5c, $\frac{\Delta c}{c}|_{2\omega}$, the sandstones have a quadratic dependence on strain for strain below 10^{-6}, while the granite and soapstone have a linear dependence on strain for strain below 10^{-6}. All samples show a decrease in the scaling of $\frac{\Delta c}{c}|_{2\omega}$ with strain for strain above 10^{-6} (see dashed line in Figure 5c). The Berea sandstone and granite exhibit the largest hysteresis in Figure 5d (large a values). This was not obvious

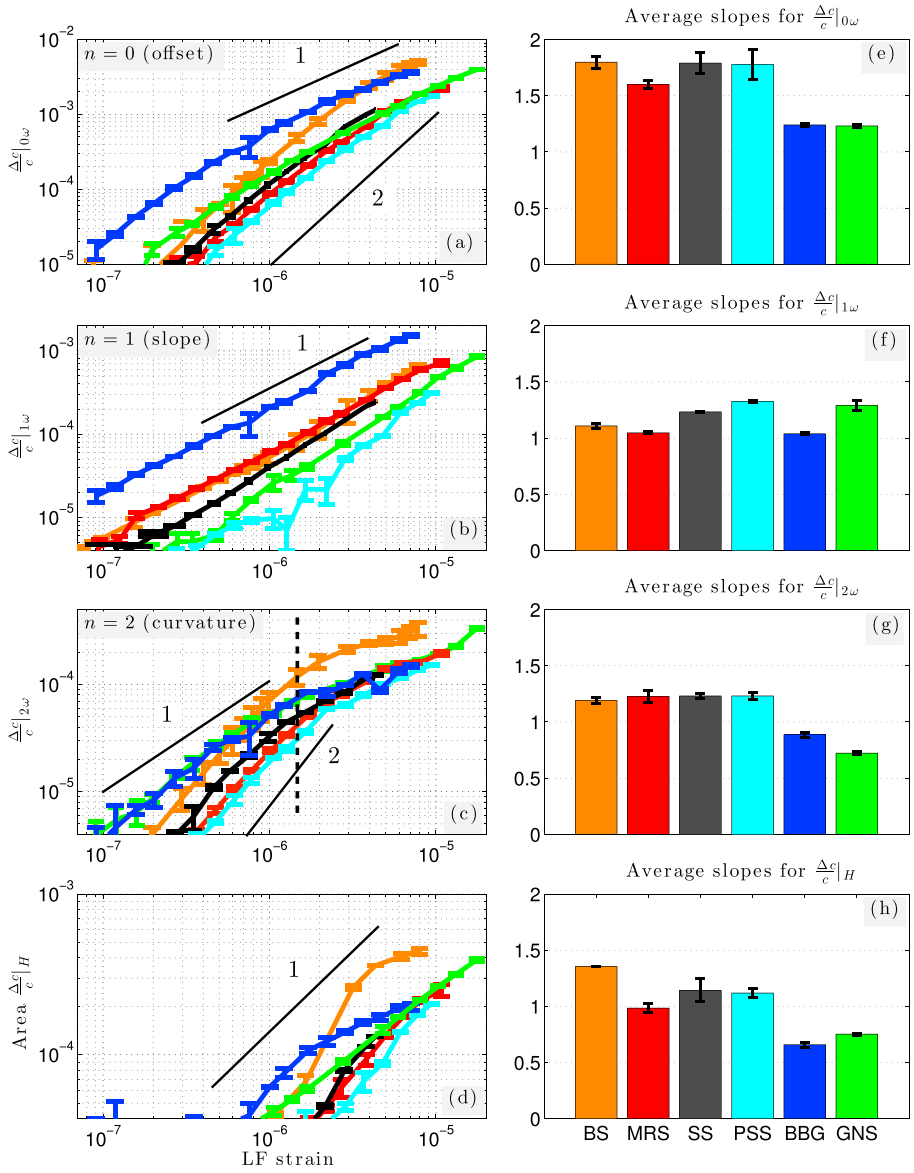

Figure 5. (left column) Amplitude dependence extracted from the projection procedure and (right column) mean slopes extracted from the amplitude dependence. BS is Berea Sandstone; MRS is Meule Red Sandstone; SS is Sander Sandstone; PSS is Pietra Serena Sandstone; BBG is Berkeley Blue Granite; GNS is Grunnes Nidaros Soapstone. (a) $\frac{\Delta c}{c}|_{0\omega}$, which corresponds to the offset in Figure 3 (averaged decrease in velocity). (b) $\frac{\Delta c}{c}|_{1\omega}$, which corresponds approximately to the slope in Figure 3. (c) $\frac{\Delta c}{c}|_{2\omega}$, which corresponds approximately to the curvature in Figure 3. (d) Hysteresis area $\frac{\Delta c}{c}|_{H}$, to estimate how different are decreasing and increasing branches of the signatures in Figure 3. (e) Mean slopes for $\frac{\Delta c}{c}|_{0\omega}$. (f) Mean slopes for $\frac{\Delta c}{c}|_{1\omega}$. (g) Mean slopes for $\frac{\Delta c}{c}|_{2\omega}$. (h) Mean slopes for the hysteresis area.

for granite on looking at the nonlinear signature in Figure 3k. The offset, curvature, and hysteresis area scale less strongly with strain for soapstone and granite than they do for the sandstones.

The coefficients ν, which describe how on average the leading components of the nonlinear signatures scale with strain, are shown in Figures 5e–5h. Before turning to an analysis which uses these average scaling coefficients we look at the NRUS data.

3.3. NRUS

In Figure 6a, we show an example of the data obtained in the NRUS measurements. The data shown in the figure is for the Grunnes Nidaros soapstone. The resonance curves for both upward sweep and downward sweep are shown. As previously observed for such experiments, the small difference between upward

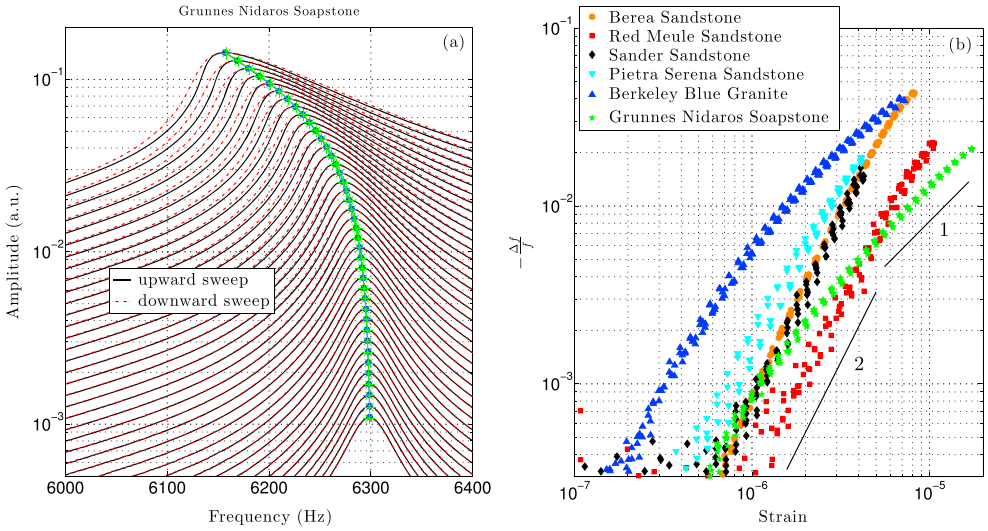

Figure 6. Nonlinear resonance ultrasound spectroscopy (NRUS). Each sample is resonated at its first compressional mode with strain amplitude ranging from 10^{-7} to 10^{-5}. (a) Typical resonance curves: example of the Grunnes Nidaros Soapstone. (b) Frequency change as a function of strain amplitude. The six runs (three upward and three downward sweeps) are displayed for each sample. Note that because $\frac{\Delta f}{f}$ is negative, $-\frac{\Delta f}{f}$ is used for this log-log plot.

and downward sweeps is due to slow dynamics [*TenCate and Shankland*, 1996; *TenCate*, 2011]. The *shift* in resonance frequency, $-\Delta f/f$, is plotted in Figure 6b as a function of the strain at resonance, ϵ_r, for all samples. The changes in frequency, $\Delta f/f$, are negative in all cases, in qualitative accord with $\Delta c/c < 0$ in the DAET measurements. These NRUS assessments of the nonlinear behavior of the samples are to be combined with the four DAET measures of nonlinear behavior from above. To capture the essentials of the NRUS data for this purpose we use the average slope of $\log(-\Delta f/f)$ as a function of $\log(\epsilon_r)$.

Table 2. Nonlinear Measures of the Average Behavior of 17 Samples Extracted From Figures 5e–5h for DAET and Figure 6b for NRUS[a]

Sample	Offset, $\mathcal{S}_1$	Slope, $\mathcal{S}_2$	Curvature, $\mathcal{S}_3$	Area, $\mathcal{S}_4$	Shift, $\mathcal{S}_5$
BS 1, $\mathcal{R}_1$	1.75	1.13	1.22	1.35	2.07
BS 2, $\mathcal{R}_2$	1.85	1.08	1.16	1.35	2.03
GNS 1, $\mathcal{R}_3$	1.24	1.36	0.71	0.74	1.21
GNS 2, $\mathcal{R}_4$	1.25	1.26	0.74	0.76	1.19
GNS 3,$\mathcal{R}_5$	1.21	1.25	0.72	0.75	1.19
MRS 1, $\mathcal{R}_6$	1.63	1.03	1.21	1.04	2.06
MRS 2, $\mathcal{R}_7$	1.61	1.05	1.16	0.94	1.80
MRS 3, $\mathcal{R}_8$	1.56	1.05	1.30	0.97	1.83
SS 1, $\mathcal{R}_9$	1.75	1.24	1.26	1.24	2.03
SS 2, $\mathcal{R}_{10}$	1.92	1.24	1.21	1.00	2.23
SS 3, $\mathcal{R}_{11}$	1.70	1.23	1.22	1.19	1.94
PSS 1, $\mathcal{R}_{12}$	1.73	1.34	1.21	1.16	1.77
PSS 2, $\mathcal{R}_{13}$	1.83	1.32	1.28	1.13	1.94
PSS 3, $\mathcal{R}_{14}$	1.78	1.33	1.21	1.07	1.95
BBG 1, $\mathcal{R}_{15}$	1.26	1.05	0.89	0.65	1.29
BBG 2, $\mathcal{R}_{16}$	1.22	1.03	0.86	0.69	1.35
BBG 3, $\mathcal{R}_{17}$	1.24	1.04	0.91	0.64	1.31

[a]The entries, displayed in Figure 7, are the exponent ν that characterizes the scaling of the log of the measured quantity with the log of the strain. For instance, for the curvature, $\log((\Delta c/c)_{2\omega}) = \nu \log(\epsilon_{1\omega}) + \log(a)$. BS is Berea Sandstone; GNS is Grunnes Nidaros Soapstone; MRS is Meule Red Sandstone; SS is Sander Sandstone; PSS is Pietra Serena Sandstone; BBG is Berkeley Blue Granite. Column vectors $\mathcal{S}_i$ and row vectors $\mathcal{R}_j$ correspond to the notation used in the text.

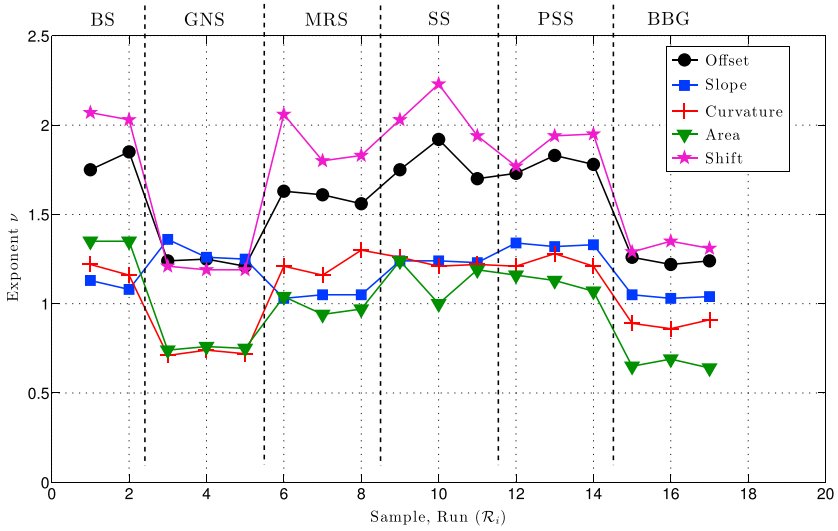

Figure 7. Exponents ν corresponding to values shown in Table 2 and extracted from Figure 5 for DAET and Figure 6b for NRUS. The entries ν characterize the scaling of the *log* of the measured quantity with the log of the strain. For instance, for the curvature, $\log((\Delta c/c)_{2\omega}) = \nu \log(\epsilon_{1\omega}) + \log(a)$. BS is Berea Sandstone; GNS is Grunnes Nidaros Soapstone; MRS is Meule Red Sandstone; SS is Sander Sandstone; PSS is Pietra Serena Sandstone; BBG is Berkeley Blue Granite.

3.4. Principal Component Analysis and Fuzzy Clustering

The projection procedure representation of DAET data was used to obtain four measures of the nonlinear behavior of each sample, offset, slope, curvature, and area. The frequency shift $\Delta f/f$ from NRUS data was used to form a fifth measure of the nonlinear behavior of each sample (called shift hereafter). The average strain dependence of these measures was captured with the scaling coefficients ν, see Figures 5e–5h. Until now (Figures 4 and 5) we have used averages over runs on each sample, e.g., two runs on Berea, three runs on Granite, etc. From here forward we regard each run on a given sample as an independent measure. Thus, we have five nonlinear measures for two Berea samples, five nonlinear measures for three Granite samples, etc. We therefore speak of $N = 17$ measurements (2 × Berea, 3 × Granite, etc). The scaling coefficients ν for each individual measurement are shown in Table 2 and Figure 7; they form a 17 × 5 matrix denoted as $\mathcal{M}$. The columns of this matrix carry information about a single measure of the nonlinear behavior across all samples, e.g., column 1 is the offset measure of the nonlinear behavior of all samples. We denote the 17 component column vectors for a measure of the nonlinear behavior by $\mathcal{S}_i, i = 1, \ldots, 5$. The rows of the $\mathcal{M}$ matrix carry information about the response of each sample to five measures of nonlinear behavior, e.g., row 1 describes the response of Berea sample 1 to five measures of nonlinear behavior. We denote the five component row vector for the nonlinear response of a sample by $\mathcal{R}_j, j = 1, \ldots, N$. The nonlinear response of a sample is a point in the five-dimensional nonlinear response space of (offset, slope, curvature, area, and shift).

We can use the data in $\mathcal{M}$ to compare measures of nonlinear behavior to one another, i.e., compare columns. Or we can use the data in $\mathcal{M}$ to compare nonlinear response from sample to sample, i.e., compare rows. There are tools available to undertake these comparisons, principal component analysis (PCA) and fuzzy clustering (FC).

PCA. We use PCA to compare nonlinear measures across samples to one another. "Does area measure something different from offset"? To answer this question we need to compare the area column vector to the offset column vector or any other column. To remove the influence of absolute values, PCA is preceded by a normalization step (see Appendix B). Thus, from each $\mathcal{S}_i$ we remove its average $\overline{\mathcal{S}_i}$ and divide by its standard deviation $\sigma_{\mathcal{S}_i}$ to form 17 component-normalized vectors, $\hat{\mathcal{S}}_i = \frac{\mathcal{S}_i - \overline{\mathcal{S}_i}}{\sigma_{\mathcal{S}_i}}$. The set of normalized vectors $\hat{\mathcal{S}}_i$ are used to construct the 5 × 5 covariance matrix

$$C_{kl} = \sum_{j=1}^{N} \hat{\mathcal{S}}_k^j \hat{\mathcal{S}}_l^j \tag{10}$$

with the upper index j running from 1 to $N=17$, i.e., the size of each $\mathcal{S}$ vector. The eigenvectors of the covariance matrix are the principal component vectors. These eigenvectors are

$$\mathbf{PC}^{\mathcal{M}} = \begin{array}{c} \begin{matrix} \mathrm{PC}_1 & \mathrm{PC}_2 & \mathrm{PC}_3 & \mathrm{PC}_4 & \mathrm{PC}_5 \end{matrix} \\ \begin{bmatrix} 0.51 & 0.08 & -0.16 & -0.44 & 0.72 \\ 0.07 & 0.97 & -0.18 & 0.10 & -0.14 \\ 0.49 & -0.19 & -0.44 & 0.73 & 0.02 \\ 0.48 & 0.10 & 0.84 & 0.21 & -0.04 \\ 0.51 & -0.12 & -0.19 & -0.47 & -0.69 \end{bmatrix} \end{array} \tag{11}$$

with the corresponding eigenvalues

$$E^{\mathcal{M}} = \begin{bmatrix} 3.6720 & 1.0447 & 0.022 & 0.010 & 0.003 \end{bmatrix}. \tag{12}$$

From E, one can calculate a cumulative sum

$$E_i^{\mathcal{M}}(\%) = \frac{\sum_{j=1}^{i} E_j}{\sum_{j=1}^{5} E_j} \times 100 \tag{13}$$

to find

$$E^{\mathcal{M}}(\%) = \begin{bmatrix} 72.0 & 94.7 & 98.0 & 99.6 & 100.0 \end{bmatrix}. \tag{14}$$

The principal component vectors $\mathrm{PC}_1, \ldots, PC_5$, five component vectors that are mutually orthonormal, lie in the nonlinear response space. The eigenvalues determine the importance of a principal component vector in describing the data in this space. We see that PC_1, corresponding to the largest eigenvalue, has very small component along the *slope* axis in nonlinear response space (0.07). It is built up of almost equal parts ($\simeq 0.5$) of the offset, curvature, area, and shift, i.e., it is approximately on the diagonal in the four-dimensional subspace of offset, curvature, area, and shift. Consequently, these four measures are of essentially the same thing. Any one of the attributes offset, curvature, area, and shift would perform equally well in capturing important features in the nonlinear response of the samples. The principal component vector PC_2, corresponding to the second largest eigenvalue, is built up almost entirely of slope (0.97), it lies almost parallel to the slope axis in the nonlinear response space. This is an indication that the nonlinear behavior captured by the slope senses very little of the physical mechanism(s) responsible for offset, curvature, area, and shift. From equation (14), we note that PC_1 and PC_2 together capture roughly 95% of variation in the data.

We will use the perspective, associated with the PCA analysis of measures of nonlinearity, to sort the samples into groups having approximately the same nonlinear response. Before doing so we call attention to a simple conclusion of our findings. The fact that the measures offset, curvature, area, and shift behave very similarly to one another across samples strongly suggests that they are due to the same physical processes in each sample (a physical process that may differ in its details from sample to sample). This greatly simplifies the construction of models for the behavior of the samples.

Fuzzy Clustering. Now let us turn to a comparison of samples according to their nonlinear response, i.e., the set of $\mathcal{R}_i$. From the PCA analysis we know that in leading approximation the nonlinear response data is well described by the first two principal component vectors, PC_1 and PC_2. Thus, we can characterize the response of sample i with the pair of numbers (X_i, Y_i), the projection of the nonlinear response vector $\mathcal{R}_i$ onto the principal component vectors PC_1 and PC_2, where $X_i = \mathcal{R}_i \cdot \mathrm{PC}_1$ and $Y_i = \mathcal{R}_i \cdot \mathrm{PC}_2$. To compare the nonlinear response of the samples we use fuzzy clustering on the 17 pairs (X_i, Y_i) (see Appendix C). We choose fuzzy clustering over k-means clustering in order to be prepared for the case that the samples are really not that different from one another. The result of fuzzy clustering analysis are shown in Figure 8 for the case that we ask for separation into two clusters.

In Figure 8 we necessarily see two clusters. What is not necessary, but is the case, is that all of the sandstone samples are in one cluster well separated from the granite and the soapstone which form a second cluster. We also see that the dots of a single color, corresponding to different runs on the same rock (2 Berea, 3 granite, etc.) overlap, suggesting the good reproducibility of the measurements. In the figure the cluster

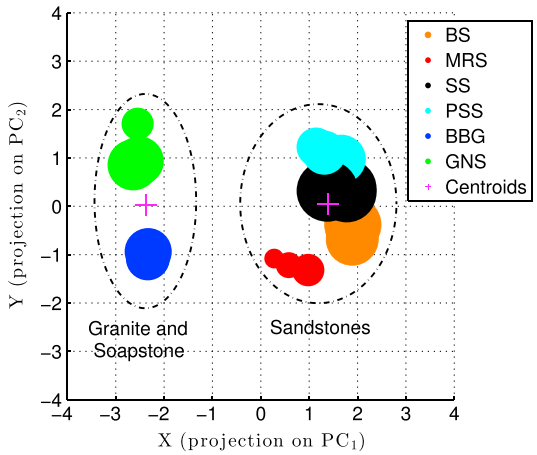

Figure 8. The results of fuzzy clustering applied to mean slopes (ν values) found in Figures 5e–5h for DAET and mean slopes extracted from Figure 6b for NRUS. The set of data is projected on the two first main components PC_1 and PC_2. The dot size is related to the membership degree of each data point to its cluster. The two crosses represent the centroids of each cluster.

centroids are shown as crosses. The size of the point for each sample is related to the membership degree of that point. The membership degree, a fuzzy clustering output, is a measure of the "confidence" with which each sample is associated with the cluster to which it is assigned (Appendix C). For the 11 samples associated with the "sandstone" cluster, the minimum membership degree is 0.93. Thus, for the case at hand fuzzy clustering suggests strong confidence in the cluster assignments.

PCA on a values. From the result above, we see that the offset, curvature, area, and shift measures vary with strain in much the same way for all samples. Albeit these measures vary differently with strain for the sandstones (the right-hand cluster in Figure 8) and for soapstone/granite (the left-hand cluster in Figure 8). If one imagines that the mechanism responsible for the nonlinear behavior seen by these measures has its source in a concentration of elastic features, e.g., defects, microcracks, etc., then it is reasonable to ask how these elastic features make themselves known in the nonlinear measures. One way to answer this question is to compare the "quantity" of elastic features in the nonlinear measures by comparing the a values associated with each sample. For instance, if the offset for Berea has larger a than the offset for Sander we might expect the curvature, the area, and the shift to have larger a values for Berea than for Sander. The slope is deliberately taken out from this analysis since we take it to arise from a different physical mechanism. Additionally, we confine ourselves to the samples in the sandstone cluster. For each of the 11 sandstone samples and for each of the four nonlinear measures we calculate a using $(-\Delta c/c)_x = a \times (\epsilon_{1_\omega})^{\overline{\nu}_x}$, where $\overline{\nu}_x$ is the average of ν for the nonlinear measure x over the 11 samples. Table 3 displays these a values. They form an 11×4 matrix denoted as $\mathcal{N}$. Our intent is to apply PCA to compare the sets of values of a from sample to sample. As the bare values of a span many orders of magnitude we form the matrix $\mathcal{LN}$ with entries that are the $\log_{10}$ of the entries in the matrix $\mathcal{N}$. Each row of $\mathcal{LN}$ is normed in the same way as the columns of $\mathcal{M}$ above. The matrix $\mathcal{LN}$, having an 11×11 covariance formed from $\mathcal{R}_i\mathcal{R}_j$ (cf. equation (10)),

Table 3. Values a Recalculated for the Set of Sandstones Using $\overline{\nu}$ Values Found for Each Nonlinear Measure[a]

Sample	Offset ($\overline{\nu} = 1.74$) ($\times 10^6$)	Curvature ($\overline{\nu} = 1.23$) ($\times 10^2$)	Area ($\overline{\nu} = 1.13$) ($\times 10^2$)	Shift ($\overline{\nu} = 1.97$) ($\times 10^8$)
BS 1	5.76	8.97	2.38	5.56
BS 2	4.47	11.35	2.74	5.56
MRS 1	1.80	3.95	1.28	1.92
MRS 2	1.88	4.20	1.38	1.90
MRS 3	2.00	3.80	1.39	1.66
SS 1	2.76	5.53	1.35	5.80
SS 2	2.50	5.78	1.49	4.75
SS 3	2.92	5.77	1.39	5.60
PSS 1	1.26	3.16	0.97	10.77
PSS 2	1.04	2.99	1.02	8.36
PSS 3	1.27	3.07	1.04	8.36

[a]BS is Berea Sandstone; MRS is Meule Red Sandstone; SS is Sander Sandstone; PSS is Pietra Serena Sandstone.

is subjected to PCA. We find that a single-principal component vector describes 95.6% of the data. The eigenvalues (compare to $E^{\mathcal{M}}$ and $E^{\mathcal{M}}(\%)$ above) are

$$E^{\mathcal{LN}} = \left[\, 3.3141 \;\; 0.1260 \;\; 0.0261 \;\; 0.0000 \,\right], \tag{15}$$

and

$$E^{\mathcal{LN}}(\%) = \left[\, 95.6 \;\; 99.2 \;\; 100.0 \;\; 100.0 \,\right]. \tag{16}$$

The single-principal component vector necessary to describe the data has equal contributions from all amplitude sets, i.e., it lies essentially on the diagonal in the 11 component space of samples. The amplitude set from any sample captures the participation of the responsible elastic features in the nonlinear measures. There are differences from sample to sample, a few percent of the logarithm, that amount to numerical factors of order 2. In particular, the Pietra Serena sandstone has a different behavior from other sandstones regarding its shift, suggesting that this sample is slightly inhomogeneous in terms of nonlinear sources, giving different results for DAET (local measurement—where the sample is probed—giving the offset, the curvature, and the area) and NRUS (bulk measurement giving the shift). Differences of this size are within the domain of sensible variations that occur in the structure of the sandstones and are not regarded as fundamental.

4. Discussion

Dynamic acoustoelasticity involves a probe strain field (a compressional strain field in the y direction, ϵ_y) that is coupled to the pump strain field (a compressional strain field in the x direction ϵ_X). The elastic energy for the system has the form

$$\mathcal{E} = \mathcal{E}_p(\epsilon_y) + K_0\hat{\beta}\epsilon_y^2\epsilon_X + \mathcal{E}_P(\epsilon_X), \tag{17}$$

where $\mathcal{E}_p$ is the elastic energy of the probe system (a linear elastic system because the probe strain is deliberately taken to be small), $\mathcal{E}_P$ is the linear plus nonlinear elastic energy of the pump system, and $\hat{\beta}$ is the strength of the pump-probe coupling. This coupling may be as simple as the cubic nonlinearity of traditional nonlinear elasticity. The equation of motion for the probe field is

$$\rho\frac{\partial^2 u_y}{\partial t^2} = \frac{\partial}{\partial y}\left(K_0(1+2\hat{\beta}\epsilon_X)\frac{\partial u_y}{\partial y}\right). \tag{18}$$

It follows that the velocity shift in the propagation of u_y, at $x = h$ at time t, is

$$\frac{\Delta c(t)}{c} = \hat{\beta}\epsilon_X(h,t), \quad \rho c^2 = K_0. \tag{19}$$

The probe field sees the *dressed* strain field, $\epsilon_X(h,t)$. The dressed strain field is built up from the *bare* strain field, the pump source strain field in equation (9), by nonlinear processes in the samples. We know from the measurements that in steady state, at pump frequency ω and bare strain field $\epsilon_{1\omega}$, the dressed strain field comprises (1) an offset strain field (a time-independent strain field), (2) a slope strain field (a strain field that moves in time with the frequency of the bare strain field), (3) a curvature strain field (a strain field that moves in time at twice the frequency of the bare strain field), and (4) an area strain field (a strain field that moves in time with the frequency of the bare strain field and is hysteretic). (We use the language developed above.) The slope strain field, moving in time with the bare strain field and having amplitude that scales approximately linearly with the amplitude of the bare strain field, is different from the offset, curvature, and area strain fields. The offset, curvature, and area strain fields, moving in time differently from the bare strain field, all have amplitudes that scales with the amplitude of the bare strain field similarly. This scaling always tends to "saturate" at large strain (see Figures 5a, 5c, 5d, and 6). For instance, when it is approximately quadratic at low strain, it becomes progressively linear at large strain. The amplitude/time dependence of the offset, curvature, and area strain fields do not have explanation within the classical theory of nonlinear elasticity, a Landau theory involving an elastic energy that is an analytic function of the strain [*Guyer and Johnson*, 2009].

We seek explanation in the domain of nonclassical nonlinearity. Generally, nonclassical nonlinear elasticity invokes the presence of unusual elastic features, e.g., hysteretic elastic elements, or the presence of elastic feature that have complex time response, e.g., the time dependence of a soft ratchet. Models involving such

features might also be expected to describe the results of an NRUS experiment and slow dynamics. We have found offset, curvature, and area to be intimately connected to NRUS in the samples we have examined. And we also see evidence of slow dynamics in all of the samples examined. The slow dynamics of the samples is to be the subject of the fourth paper in this series. Hysteretic behavior arises in models in which elastic elements are described by a Preisach space bookkeeping space. The simplest example of such a model is that of McCall and Guyer [*Guyer and Johnson*, 2009; *McCall and Guyer*, 1994]. In this model there is hysteresis with the hysteresis loop area that is connected to the frequency shift seen in NRUS. There is also a modulus shift (offset). However, this offset is caused by the dynamics of elastic wave motion which sees it and is not a condition of the sample that would be felt by a probe. So we would say that the McCall-Guyer model could describe some features that are in the nonclassical nonlinear response. But it would miss at least one very important feature, the offset. Our results show that the NRUS shift and the offset are strongly correlated, having very similar ν values as seen in Figure 7. This demonstrates that measuring the offset with DAET is similar to measuring a frequency shift with NRUS (as previously observed for a sample of Lavoux Limestone in *Renaud et al.* [2013a]). Future modeling efforts will have to account for the fact that these two quantities are strongly related and most likely represent the same physical phenomenon. A recent model by Lebedev and Ostrovsky [*Lebedev and Ostrovsky*, 2014] was deliberately constructed to tie slow dynamics to hysteretic behavior. This model, involving the system being held in a nonequilibrium steady state by the dynamics, has the possibility of offering a qualitative understanding of NRUS and slow dynamics. An even more recent model [*Favrie et al.*, 2014] builds on the soft ratchet ideas introduced by *Vakhnenko et al.* [2005] and leads to qualitative results similar to those seen in these experiments, i.e., offset, curvature, area, and slow dynamics. Models [*Aleshin and Van Den Abeele*, 2007; *Lawn and Marshall*, 1998; *Nihei et al.*, 2000; *Pecorari*, 2004] based on friction and/or adhesion in materials containing cracks (therefore, more physical and less phenomenological) or inspired by dislocation theories in metals [*Pecorari*, 2014, 2015] can produce hysteretic behavior similar to what we observe, although they do not connect hysteretic behaviors with slow dynamics. Part of future modeling efforts will be to merge these models to achieve a fully physical-based description. It is not our intention to fit the data described in this paper to any of these models. We do suggest that they may be appropriate to the data. However, our intention is to make available data sets of unprecedented quality to serve as a testing ground for these theories.

5. Conclusion

Dynamic acoustoelasticity tests have been conducted on a set of six samples, four sandstones, one soapstone, and one granite. These samples allow comparison of sedimentary and metamorphic rocks (sandstones/soapstone) with a crystalline rock (granite). This paper is the third in a series that develops DAET for geophysical applications [*Renaud et al.*, 2012; *Rivière et al.*, 2013]. Each sample is probed at 20 strain amplitudes logarithmically distributed over 2 orders of magnitude, $10^{-7} < \epsilon < 10^{-5}$. A projection procedure developed in [*Rivière et al.*, 2013] allows us to decompose the complex signatures of nonlinear elasticity into a set of four measures of nonlinearity. To these four measures of nonlinear behavior from DAET we add a fifth from the results of NRUS measurements. We employ statistical tools to provide a systematic analysis to these measures. For instance, it is found that the slope of the signatures is associated to physical processes different from the ones associated with the offset, the curvature, and the area of the signatures. The three latter features are essentially arising from the same physical mechanisms in each sample (not necessarily the same physical processes in all samples). In addition, the frequency shift measured with NRUS also correlates with these three last features. Using such result, we then apply the fuzzy clustering technique to compare these features among samples. We found that the set of sandstones cluster together, whereas granite and soapstone form the second cluster. In a second step, we try to see if, among the sandstones, the same mechanism is responsible for the offset, the curvature, the area, and the shift. This second analysis indeed suggests that the quantity of elastic features (a values) are consistent with the assumption of a single mechanism explaining these four nonlinear measures.

Finally, DAET provides new insights on nonlinear elasticity that will ultimately contribute to the development of physically based theories, enabling to link the nonlinear elastic response to damage features. This work aims at starting a DAET database, and more samples with more diverse damage features will have to be studied in order to reach a more complete view on physical processes associated with the nonlinear elastic responses. In addition, nonlinear measures extracted from the relaxation curves (see postpump excitation in Figure 2b) will also be added to the database in future work.

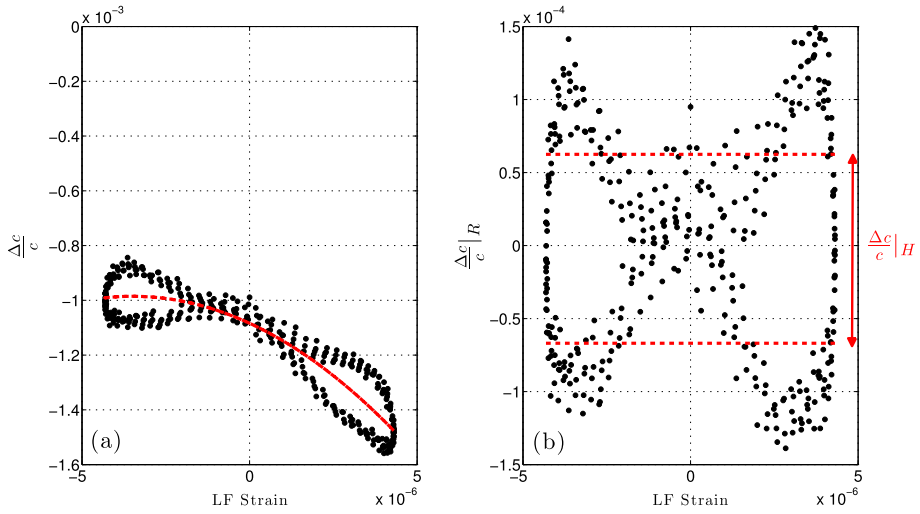

Figure A1. Estimation of the hysteresis area $\frac{\Delta c}{c}|_H$. (a) Example of second-order polynomial applied to a nonlinear signature. (b) "Bow tie" signature $\frac{\Delta c}{c}|_R$ resulting from the subtraction between the original data and the second-order polynomial fit. The area $\frac{\Delta c}{c}|_H$ is then defined as the difference between averaged positive values and averaged negative values: $\frac{\Delta c}{c}|_H = \overline{\frac{\Delta c}{c}|_R > 0} - \overline{\frac{\Delta c}{c}|_R < 0}$.

Appendix A: Hysteresis Estimation

The hysteresis area is estimated using a polynomial representation. A second-order polynomial $(a\epsilon_{1\omega}^2 + b\epsilon_{1\omega} + c)$ is fitted to each nonlinear signature in Figure 3. This fit is then subtracted from the nonlinear signature to produce $\frac{\Delta c}{c}|_R$ (see Figure A1). When hysteresis is present this subtraction results in a symmetric "bow tie" centered at the $\Delta c/c - \epsilon_{1\omega}$ origin. We calculate the average of all of the positive values $\overline{\frac{\Delta c}{c}|_R > 0}$ and the average of all of the negative values $\overline{\frac{\Delta c}{c}|_R < 0}$ and define the hysteresis area to be $\frac{\Delta c}{c}|_H = \overline{\frac{\Delta c}{c}|_R > 0} - \overline{\frac{\Delta c}{c}|_R < 0}$. When high harmonic content is present in the nonlinear signatures (for instance, at the largest strain amplitude in Figures 3a and 3i), a fourth-order polynomial is sometimes used in making the estimate of $\frac{\Delta c}{c}|_R$.

Appendix B: Principal Component Analysis

PCA is an analysis used to reduce the dimension of a complex data matrix. Reducing the dimension is to help accelerate further data processing steps or facilitate visualization. This is achieved by revealing the redundancies (correlated attributes) in the data set, which may otherwise obscure the patterns and structures of interest in the data. Mathematically speaking, PCA is an orthogonal linear transformation that projects the data onto a new orthogonal base by minimizing the projection errors. As a consequence, the variance in the data is maximum along the first projection direction (called the first principal component), second greatest along the second direction or the second principal component (normal to the first principal component), and so on. There can be as many principal components as there are attributes (or variables) in the data set, ranked in the decreasing order based on the amount of variation they capture in the data. However, only a relatively (with respect to the matrix original dimension) small number of principal components is usually sufficient to reconstruct the data matrix, retaining 95–100% of the variation in the data. To obtain the principal components, we can use the eigenvalue decomposition of the data covariance (or cross-correlation) matrix or singular value decomposition of the data, usually after having properly normalized the data. For example, by zero meaning, rescaling, or *z* transform. For a detailed discussion on PCA, see, for instance, *Jolliffe* [2005]. Prior to performing PCA in this study, we have normalized the data by zero meaning and rescaling (dividing by standard deviation) to a common range. This normalization allows one to capture differences between the different samples rather than differences in mean slope for the different measures.

Appendix C: Clustering

Clustering is one of the most important *unsupervised machine learning* algorithms. This class of algorithms attempt to *learn* and extract hidden structures in unlabeled data. Unlike supervised learning algorithms, no training data set (i.e., labeled data) is needed. In simple terms, clustering algorithms divide the data set into subsets called clusters by assigning similar data into one cluster. The data points grouped in one cluster are most similar to each other and dissimilar to the data points in the neighboring clusters based on a predefined similarity criterion. The similarity is typically measured in the form of a multidimensional distance function.

C1. *K*-Means Clustering

K-means algorithm [*MacQueen*, 1967] is the simplest clustering approach. Consider a data set consisting of N q-dimensional data points x_i describing the values of q parameters measured for N samples. One may use *K*-means clustering to see if the samples could be partitioned into K distinct subsets based on the similarities between the corresponding measurements. This algorithm assigns the q-dimensional data points x_i to K distinct clusters with q-dimensional centroids C_j $j=1,\ldots,K$ such that the total sum of the distances between the data points within each cluster and the corresponding cluster centroids is minimized:

$$\min \sum_{j=1}^{K} \sum_{i=1}^{N} \mathrm{dist}(x_i - C_j)^2 \tag{C1}$$

where *dist* is an appropriate distance function. One popular choice is the Euclidian distance. Please note that the number of clusters K is chosen a priori.

C2. Fuzzy *C*-Means Clustering

Fuzzy clustering (aka soft *K*-means) is a variation of *K*-means clustering, where each piece of data can simultaneously belong to two or more clusters. The degree of belonging of x_i to cluster j is described by a membership function $m_{i(j)}$. The Fuzzy *c*-means clustering algorithm was first proposed by *Dunn* [1973] and later modified by *Bezdek et al.* [1981]. It is based on the minimization of the following objective function:

$$\min \sum_{j=1}^{K} \sum_{i=1}^{N} m_{i(j)}^{\alpha} \mathrm{dist}(x_i - C_j)^2 \tag{C2}$$

where α is a real number not smaller than 1. The optimization is achieved iteratively by updating the cluster centroid C_j and the membership $m_{i(j)}$ as follows:

$$C_j = \frac{\sum_{i=1}^{N} m_{i(j)}^{\alpha} x_i}{\sum_{i=1}^{N} m_{i(j)}^{\alpha}} \tag{C3}$$

$$m_{i(j)} = \frac{1}{\sum_{k=1}^{K} \frac{\mathrm{dist}(x_i - C_j)}{\mathrm{dist}(x_i - C_k)}^{\frac{2}{\alpha-1}}} \tag{C4}$$

Acknowledgments
We thank G. Renaud, S. Haupert, J. A. TenCate, T. Shankland, P.-Y. Le Bas, and T. J. Ulrich, for fruitful discussions and J. Wilson for her help with photomicrographs. This work is supported by the U.S. Department of Energy, Office of Basic Energy Sciences. The current policies of Los Alamos National Laboratory do not allow the public release of experimental data presented in this study. For more information, please contact the authors.

References

Aleshin, V., and K. E. A. Van Den Abeele (2007), Friction in unconforming grain contacts as a mechanism for tensorial stress–strain hysteresis, *J. Mech. Phys. Solids*, *55*(4), 765–787.

Bezdek, J., C. Coray, R. Gunderson, and J. Watson (1981), Detection and characterization of cluster substructure I. Linear structure: FUZzy *c*-lines, *SIAM J. Appl. Math.*, *40*(2), 339–357.

Bouchaala, F., C. Payan, V. Garnier, and J. Balayssac (2011), Carbonation assessment in concrete by nonlinear ultrasound, *Cem. Concr. Res.*, *41*(5), 557–559.

Cespedes, I., Y. Huang, J. Ophir, and S. Spratt (1995), Methods for estimation of subsample time delays of digitized echo signals, *Ultrasonic Imaging*, *17*(2), 142–171.

Dunn, J. (1973), A fuzzy relative of the isodata process and its use in detecting compact well-separated clusters, *J. Cybern.*, *3*, 32–57.

Favrie, N., B. Lombard, and C. Payan (2014), Fast and slow dynamics in a nonlinear elastic bar excited by longitudinal vibrations, arXiv preprint arXiv:1412.2979.

Guyer, R., and P. Johnson (2009), Nonlinear mesoscopic elasticity: The complex behaviour of rocks, soil, concrete, 395 pp.

Haupert, S., G. Renaud, J. Rivière, M. Talmant, P. A. Johnson, and P. Laugier (2011), High-accuracy acoustic detection of nonclassical component of material nonlinearity, *J. Acoust. Soc. Am.*, *130*, 2654–2661.

Jolliffe, I. (2005), *Principal Component Analysis*, Wiley Online Lib., New York.

Lawn, B. R., and D. B. Marshall (1998), Nonlinear stress-strain curves for solids containing closed cracks with friction, *J. Mech. Phys. Solids*, *46*(1), 85–113.

Lebedev, A., and L. Ostrovsky (2014), A unified model of hysteresis and long-time relaxation in heterogeneous materials, *Acoust. Phys.*, *60*(5), 555–561.

MacQueen, J. (1967), Some methods for classification and analysis of multivariate observations, in *Proc. of the Fifth Berkeley Symposium on Mathematical Statistics and Probability*, vol. 1, edited by L. M. Le Cam and J. Neyman, pp. 281–297, Univ. of Calif. Press, Berkeley, Calif.

McCall, K., and R. Guyer (1994), Equation of state and wave propagation in hysteretic nonlinear elastic materials, *J. Geophys. Res.*, *99*, 23,887–23,897.

Meegan, G. D., P. A. Johnson, R. A. Guyer, and K. R. McCall (1993), Observations of nonlinear elastic-wave behavior in sandstone, *J. Acoust. Soc. Am.*, *94*, 3387–3391.

Nihei, K., L. Hilbert Jr., N. Cook, S. Nakagawa, and L. Myer (2000), Frictional effects on the volumetric strain of sandstone, *Int. J. Rock Mech. Min. Sci.*, *37*(1), 121–132.

Pasqualini, D., K. Heitmann, J. A. TenCate, S. Habib, D. Higdon, and P. A. Johnson (2007), Nonequilibrium and nonlinear dynamics in Berea and Fontainebleau sandstones: Low-strain regime, *J. Geophys. Res.*, *112*, B01204, doi:10.1029/2006JB004264.

Payan, C., V. Garnier, J. Moysan, and P. A. Johnson (2007), Applying nonlinear resonant ultrasound spectroscopy to improving thermal damage assessment in concrete, *J. Acoust. Soc. Am.*, *121*, 125–130, doi:10.1121/1.2710745.

Pecorari, C. (2004), Adhesion and nonlinear scattering by rough surfaces in contact: Beyond the phenomenology of the Preisach–Mayergoyz framework, *J. Acoust. Soc. Am.*, *116*(4), 1938–1947.

Pecorari, C. (2014), Modeling the elasto-acoustic hysteretic nonlinearity of dry Berea sandstone, *Wave Motion*, *52*, 66–80.

Pecorari, C. (2015), One-dimensional nonlinear scattering by localized hysteretic damage and its application to damage characterization, *Ultrasonics*, *57*, 96–103.

Renaud, G., S. Callé, and M. Defontaine (2009), Remote dynamic acoustoelastic testing: Elastic and dissipative acoustic nonlinearities measured under hydrostatic tension and compression, *Appl. Phys. Lett.*, *94*, 011905, doi:10.1063/1.3064137.

Renaud, G., S. Callé, and M. Defontaine (2010), Dynamic acoustoelastic testing of weakly pre-loaded unconsolidated water-saturated glass beads, *J. Acoust. Soc. Am.*, *128*, 3344–3354.

Renaud, G., M. Talmant, S. Callé, M. Defontaine, and P. Laugier (2011), Nonlinear elastodynamics in micro-inhomogeneous solids observed by head-wave based dynamic acoustoelastic testing, *J. Acoust. Soc. Am.*, *130*(6), 3583–3589.

Renaud, G., P. Le Bas, and P. Johnson (2012), Revealing highly complex elastic nonlinear (anelastic) behavior of Earth materials applying a new probe: Dynamic acoustoelastic testing, *J. Geophys. Res.*, *117*, B06202, doi:10.1029/2011JB009127.

Renaud, G., J. Rivière, S. Haupert, and P. Laugier (2013a), Anisotropy of dynamic acoustoelasticity in limestone, influence of conditioning, and comparison with nonlinear resonance spectroscopy, *J. Acoust. Soc. Am.*, *133*, 3706–3718.

Renaud, G., J. Rivière, P. Le Bas, and P. Johnson (2013b), Hysteretic nonlinear elasticity of Berea sandstone at low vibrational strain revealed dy dynamic acousto-elastic testing, *Geophys. Res. Lett.*, *40*, 715–719, doi:10.1002/grl.50150.

Renaud, G., J. Rivière, C. Larmat, J. Rutledge, R. Lee, R. Guyer, K. Stokoe, and P. Johnson (2014), In situ characterization of shallow elastic nonlinear parameters with dynamic acoustoelastic testing, *J. Geophys. Res. Solid Earth*, *119*, 6907–6923, doi:10.1002/2013JB010625.

Rivière, J., G. Renaud, R. Guyer, and P. Johnson (2013), Pump and probe waves in dynamic acousto-elasticity: Comprehensive description and comparison with nonlinear elastic theories, *J. Appl. Phys.*, *114*, 054905.

Scalerandi, M., S. Idjimarene, M. Bentahar, and R. El Guerjouma (2014), Evidence of microstructure evolution in solid elastic media based on a power law analysis, *Commun. Nonlinear Sci. Numer. Simul.*, *22*, 334–347.

TenCate, J. (2011), Slow dynamics of Earth materials: An experimental overview, *Pure Appl. Geophys.*, *168*(12), 2211–2219.

TenCate, J., and T. Shankland (1996), Slow dynamics in the nonlinear elastic response of Berea sandstone, *Geophys. Res. Lett.*, *23*, 3019–3022.

Vakhnenko, O., V. Vakhnenko, and T. Shankland (2005), Soft-ratchet modeling of end-point memory in the nonlinear resonant response of sedimentary rocks, *Phys. Rev. B*, *71*, 174103.

Van Den Abeele, K. E. A., and J. De Visscher (2000), Damage assessment in reinforced concrete using spectral and temporal nonlinear vibration techniques, *Cem. Concr. Res.*, *30*, 1453–1464.

Van Den Abeele, K. E. A., P. Johnson, R. Guyer, and K. McCall (1997), On the quasi-analytic treatment of hysteretic nonlinear response in elastic wave propagation, *J. Acoust. Soc. Am.*, *101*, 1885–1898.

Van Den Abeele, K. E. A., J. Carmeliet, J. A. Ten Cate, and P. A. Johnson (2000a), Nonlinear elastic wave spectroscopy (news) techniques to discern material damage, part II: Single-mode nonlinear resonance acoustic spectroscopy, *Res. Nondestr. Eval.*, *12*, 31–42.

Van Den Abeele, K. E. A., P. Johnson, and A. Sutin (2000b), Nonlinear elastic wave spectroscopy (NEWS) techniques to discern material damage, Part I: Nonlinear wave modulation spectroscopy (NWMS), *Res. Nondestr. Eval.*, *12*, 17–30.

Van Den Abeele, K. E. A., W. Desadeleer, G. De Schutter, and M. Wevers (2009), Active and passive monitoring of the early hydration process in concrete using linear and nonlinear acoustics, *Cem. Concr. Res.*, *39*, 426–432, doi:10.1016/j.cemconres.2009.01.016.

Winkler, K., and L. McGowan (2004), Nonlinear acoustoelastic constants of dry and saturated rocks, *J. Geophys. Res.*, *109*, B10204, doi:10.1029/2004JB003262.

Xu, H., S. Day, and J.-B. H. Minster (1998), Model for nonlinear wave propagation derived from rock hysteresis measurements, *J. Geophys. Res.*, *103*(B12), 29,915–29,929.